

Research Article

Automatic Classification of Red Blood Cell Morphology Based on Quantitative Phase Imaging

Mengduo Jiang,¹ Meng Shao,¹ Xiao Yang,¹ Linna He,¹ Tao Peng,¹ Tao Wang,¹ Zeyu Ke,¹ Zixin Wang,¹ Shu Fang,¹ Yuxin Mao,¹ Xilin Ouyang ,² Gang Zhao ,³ and Jinhua Zhou ^{1,4}

¹School of Biomedical Engineering, Anhui Medical University, Hefei 230032, China

²The Fourth Medical Center, Chinese PLA General Hospital, Beijing 100037, China

³The Department of Electronic Science and Technology, University of Science and Technology of China, Hefei 230027, China

⁴3D Printing and Tissue Engineering Center, Anhui Provincial Institute of Translational Medicine, Anhui Medical University, Hefei 230032, China

Correspondence should be addressed to Xilin Ouyang; ouy70301@sina.com, Gang Zhao; zhaog@ustc.edu.cn, and Jinhua Zhou; zhoujinhua@ahmu.edu.cn

Received 11 November 2021; Accepted 8 March 2022; Published 18 April 2022

Academic Editor: Nicusor Iftimia

Copyright © 2022 Mengduo Jiang et al. This is an open access article distributed under the Creative Commons Attribution License, which permits unrestricted use, distribution, and reproduction in any medium, provided the original work is properly cited.

Classification of the morphology of red blood cells (RBCs) plays an extremely important role in evaluating the quality of long-term stored blood, as RBC storage lesions such as transformation of discocytes to echinocytes and then to spherocytes may cause adverse clinical effects. Most RBC segmentation and classification methods, limited by interference of staining procedures and poor details, are based on traditional bright field microscopy. In the present study, quantitative phase imaging (QPI) technology was combined with deep learning for automatic classification of RBC morphology. QPI can be used to observe unstained RBCs with high spatial resolution and phase information. In deep learning based on phase information, boundary curvature is used to reduce inadequate learning for preliminary screening of the three shapes of unstained RBCs. The model accuracy was 97.3% for the stacked sparse autoencoder plus Softmax classifier. Compared with the traditional convolutional neural network, the developed method showed a lower misclassification rate and less processing time, especially for RBCs with more discocytes. This method has potential applications in automatically evaluating the quality of long-term stored blood and real-time diagnosis of RBC-related diseases.

1. Introduction

During long-term storage of blood, the morphology of red blood cells (RBCs) undergoes a deterioration process wherein discocytes are transformed into echinocytes and then into spherocytes [1]. The biochemical and biophysical changes in this process are termed as RBC storage lesions [2]. Such changes are also detected in cell aging [3], suggesting a relevance between RBC morphological changes and cell aging [4]. In the process of RBC aging, the deformability of RBCs is weakened, and the fragility of RBCs is enhanced [5, 6], which may cause changes in RBC function, leading to adverse clinical outcomes such as

increased postoperative infection, deep vein thrombosis, and multiorgan failure [7]. Therefore, statistical analysis of the distribution of RBC morphology is crucial to evaluating the quality of stored RBCs. Based on cell morphology analysis, this RBC classification method can also provide diagnostic information on blood diseases [8, 9].

With the development of computer language and artificial intelligence, the classification algorithms based on machine learning [10–17] have enabled rapid, efficient, and automatic classification of RBCs. However, in the majority of previous studies, the extraction of morphological features of RBCs is manually screened, which is time-consuming and requires prior knowledge. Moreover, most RBC automatic

classification methods are based on traditional bright field imaging technologies. In these imaging methods, due to the small optical absorption coefficient and poor imaging contrast of RBCs, the microscopic image of unstained RBCs is not clear enough to provide enough details to distinguish among discocytes and spherocytes. As a result, the quantitative measurement methods based on morphological analysis of RBCs [18, 19] have been applied to increase the staining-free RBC automatic classification accuracy.

Quantitative phase imaging (QPI) is a widely applied quantitative measurement method of analyzing staining-free translucent or transparent samples [20]. It can be realized by digital holography microscopy (DHM) [21], quantitative differential phase contrast (DPC) [22], or transport of intensity equation (TIE) methods [23]. As a quantitative phase imaging technology, the hologram obtained by DHM was reconstructed by digital simulation to recover QPI, which can be used to analyze the morphology of RBCs [19, 21, 24]. However, off-axis DHM requires high resolution of recording materials and high position accuracy of reconstructed light. Similarly, TIE imaging requires multiple scans, which is time-consuming and difficult to achieve real-time imaging of biological samples. Different from DHM and TIE, DPC is only calculated from two symmetrical oblique illumination [25] images by phase transfer function, and then, QPI is recovered by deconvolution. In this method, the imaging device is simple, and the imaging process is fast.

In this study, we described an automatic RBC classification approach in which the oblique illumination (OI) images of the RBCs were recorded using coded LED array microscopy and the corresponding phase images were reconstructed from DPC images using phase recovery techniques. Specifically, we introduced the stacked sparse autoencoder (SSAE) that used a full connection model for high-level feature learning, thus to reduce processing time. The SSAE was trained from bottom-up in an unsupervised manner to extract hidden features, and efficient representation of the features in turn enabled more accurate and supervised classification. To increase the accuracy of classification, our proposed method included a boundary descriptor known as boundary curvature (BC), which considered the irregularity and diversity in cell boundaries.

2. Materials and Methods

Figure 1 shows the flowchart of the combination of BC and SSAE to achieve RBC classification. First, microscopic images were obtained by the phase reconstruction method in Section 2.1, and images with only single RBC were obtained by the segmentation and extraction method in Section 2.3. Next, the massive single-cell images were divided into three categories of raw data x automatically according to the dataset preparation method in Section 2.4. In the training phase, the different original datasets x of RBCs, which were automatically divided into different classification categories (discocyte, echinocyte, and spherocyte) by the classification hyperplane, were input into SAE1 of SSAE to obtain the activation value h_1 and parameter W . Similarly, h_2 , which

was obtained by inputting h_1 and W into SAE2, was input into the Softmax classifier. To increase the accuracy of the model, x , h_1 , and h_2 were reloaded into SSAE for fine tuning [26] to minimize L , the process of which was called as the deep neural network (DNN). In the testing phase, BC in Section 2.5 was used to preliminarily screen the RBC phase images. After this screening, the images were input into the DNN to obtain the morphological features of RBC. According to results from the DNN, their probabilities were mapped by the Softmax classifier, as given in Section 2.6; then, the possibility of RBC classification was achieved. This combination of SSAE and BC can learn the morphological characteristics and facilitate the classification of RBCs.

2.1. Experimental Device. In a commercial inverted fluorescence microscope (Olympus IX73, Tokyo, Japan), the halogen lamp was replaced with an LED array (red, green, and blue primary colors, WS2812B, China). We selected green light (the wavelength at 515–530 nm) as the experimental light source. The distance of adjacent LED within the array is 8.3 mm, and the highest power of the LED array is 4.096 w, as shown in Figure 2(a). The LED array was fixed on a 3D printed bracket. Its lightening pattern was controlled by signals from a programmable system-on-chip (PSoC, CY8CKIT-059, USA). When light rays from the LED array illuminated the sample at a specific angle, the transmitted light passing through an objective (40X, NA = 0.75, Olympus) was projected on a charge-coupled (CCD) camera. The CCD (Mindvision, MV-SUA231GM-T, China) has the resolution of 1920 pixels \times 1200 pixels.

The imaging modes can be switched by illuminations patterns. Bright field (BF) images can be obtained by lightening the entire LED array. If half of the LED array (top, bottom, left or right) is lightened, as shown at the top of Figure 2(b), the corresponding OI images are I_T , I_B , I_L , and I_R , respectively. For a set of OI images (I_L and I_R) with complementary illumination angles in the vertical direction, the DPC image is calculated by [27]

$$I_{LR}^{DPC} = \frac{I_L - I_R}{I_L + I_R}. \quad (1)$$

Then, the DPC image I_{TB}^{DPC} is determined by the pairwise complementary OI images (I_T and I_B) in the horizontal direction according to equation (1). According to the weak object transfer function (WOTF) and the Tikhonov criterion [23], the phase of the QPI image can be determined. The detailed phase can be described as [27]

$$\varphi(r) = F^{-1} \left\{ \frac{\sum_i [PTF_i^{DPC*}(u) \cdot I_i^{DPC}(u)]}{\sum_i |PTF_i^{DPC*}(u)|^2 + \alpha} \right\}, \quad (2)$$

where F^{-1} denotes the inverse Fourier transform, and $PTF_i^{DPC*}(u)$ and $I_i^{DPC}(u)$ represent the conjugate of phase transfer function on different axes and the Fourier spectrum of DPC image, respectively. The sign of i stands for the amount of axis from multiaxis DPC, where $i = 2$, indicating two axial distributions (horizontal and vertical directions). α is a parameter for Tikhonov regularization.

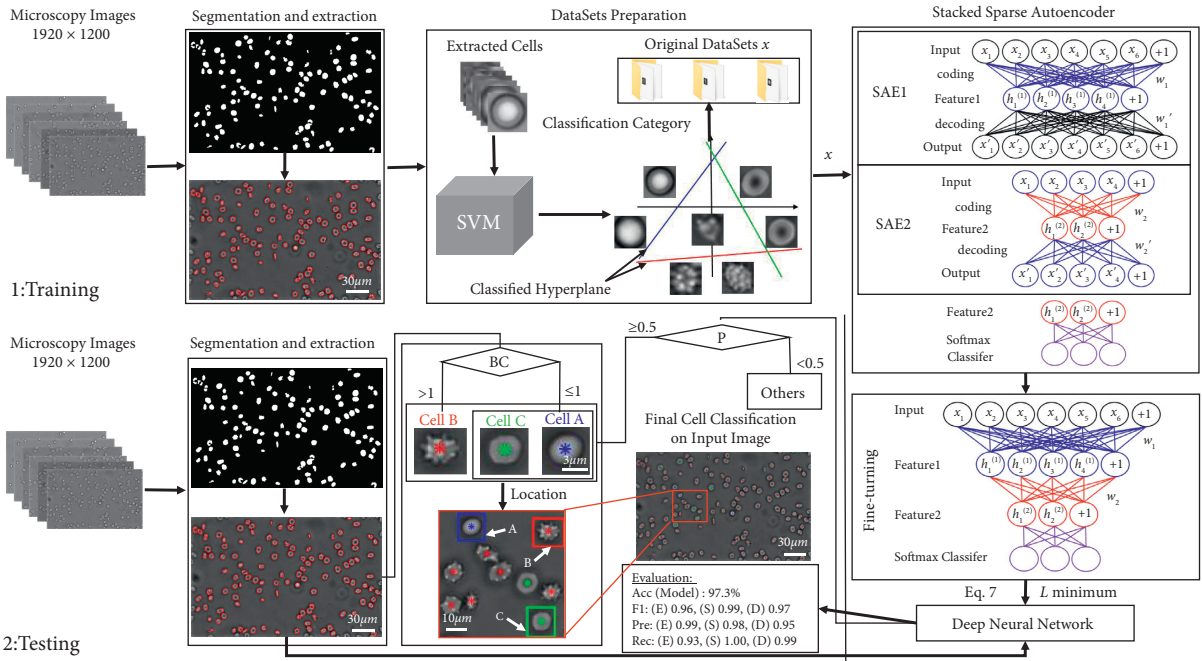


FIGURE 1: Schematic illustration of the RBC classification process. The process is divided into two stages: training and testing. In the training phase, the model of SSAE trained by the original image block is fine tuned to obtain the DNN. In the testing phase, the BC, DNN, and Softmax classifier are used to classify the cells in the unknown images, where cells A, B, and C are the spherocyte, echinocyte, and discocyte in the prediction results, respectively.

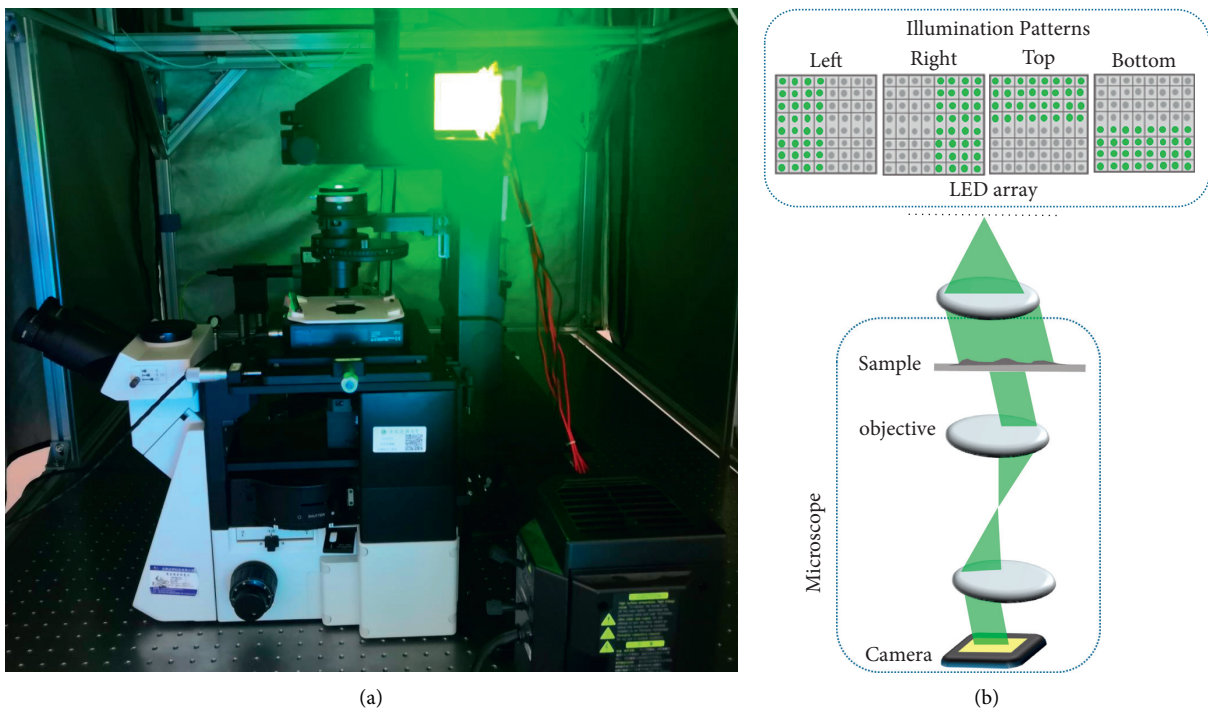


FIGURE 2: Microscopic imaging device and method. (a) A microscope with a coded LED array for illumination. (b) Imaging from time-shared oblique illumination.

2.2. RBC Sample. RBC samples were collected from healthy donors (aged 18–30 years). To understand the morphological changes of RBCs during storage, a 5 ml whole blood sample was obtained through the vein and stored in the

CPDA-1 solution at the ratio of 1.4 : 10, and then, the sample was then preserved in a refrigerator at $4^{\circ}\text{C} \pm 2^{\circ}\text{C}$. The morphology of RBCs was altered by adjusting the osmotic pressure on phosphate buffer saline (PBS) [28]. For each

sample preparation, 10X PBS (Spark Jade, CR0015-500 ML, China), 1X PBS (Spark Jade, CR0014-500 ML, China) with pH 7.1, and deionized water were mixed to obtain a specific PBS with different osmotic pressures. The whole blood sample was diluted with PBS at 1:100. The dominated morphologies of RBCs in hypertonic PBS (628 mOsm), isotonic PBS (300 mOsm), and hypotonic PBS (148 mOsm) are the echinocytes, discocytes, and spherocytes, respectively. To obtain the three shapes of RBCs in the same image, we blended the blood stored for 4 weeks with fresh blood in isotonic PBS, where the environmental temperature was kept at 22°C during the experiment.

2.3. RBC Segmentation. The preprocessing step of cell segmentation is essential for RBC classification, recognition, and tracking [29, 30]. The connected domain segmentation algorithm can easily lead to inaccurate segmentation due to cell adhesion [31, 32]. The watershed segmentation algorithm based on connected domain analysis is an extension of the connected domain segmentation algorithm [33], which can separate the target of partial adhesion. First, the images were preprocessed by gray processing and bilateral filtering [34] to reduce the influence of background noise on cell segmentation. Second, the preprocessed images were processed by adaptive threshold, dilation, erosion, and morphological filtering, which could reduce the influence of noncellular substances on segmentation. Finally, the watershed algorithm was applied to the binary images to solve the phenomenon of partial cell adhesion. In the process of extracting RBCs, the preprocessing algorithm can achieve the purpose of edge-preserving denoising due to the consideration of spatial information and gray-scale similarity, and the simple and fast Otsu method [35] is not affected by image brightness and contrast.

2.4. Dataset Preparation. For training the network model to learn the morphological features of RBCs, the datasets of the three shapes of RBCs need to be prepared. A subjective error might generate unavoidably if the dataset is prepared manually [36]. To solve this problem, we used the support vector machine (SVM) [37], which needed only a small sample (the three shapes of RBCs selected by experienced biologist experts in Section 3.3) to determine the classification hyperplane, quickly and efficiently. Figure 3 shows the process of RBC dataset preparation. First, the known single RBCs were trained by SVM to form a classification hyperplane, which was the classification label after feature learning. Second, the unknown single RBCs were then predicted by the classification hyperplane. Finally, the dataset was prepared after manual inspection. Our method not only reduced manual subjective error but also saved resources (Section 3.3). Different shapes of single RBC images rotated 90°, 180°, 270°, and 360° and flipped could be magnified up to six times of the original images [38], which constituted the dataset for training and testing in Section 2.6 and further enhanced the robustness of the classification model to increase classification accuracy.

2.5. Extraction of RBC Features

2.5.1. Boundary Curvature. During the process of cell aging, the morphology of echinocyte changes from disco-echinocyte to echinoco-spherocyte [39], and the irregularity and diversity of RBC morphology may lead to incomplete feature learning [40]. Tangent count can be applied to estimate the change in the concavity and convexity of “contour” of RBCs [41]; however, the tangent point is so important that inaccurate positioning may lead to misjudgment. Accordingly, we introduced an edge-based descriptor, termed BC, which was an extension of tangent count. It is beneficial to reduce the dependence on sampling location with this descriptor because the target is uniformly sampled to judge whether the boundary of the cell is smooth. BC is defined as the rate of change of slope. Generally speaking, when moving clockwise on the boundary, if the slope change rate of point P is not negative, P is a part of the convex line segment; otherwise, P belongs to the concave line segment. To obtain BC of RBC, we need to obtain the boundary coordinates, that is, the coordinates of sampling points are $(x_1, y_1), (x_2, y_2), \dots, (x_n, y_n)$, where $1 \leq n \leq C$, and C is the perimeter of the boundary cell. The slope of adjacent points is expressed as follows:

$$k_i = \frac{y_{i+1} - y_i}{x_{i+1} - x_i} \quad (3)$$

Thus, the number of negative values of BC is given as follows [42]:

$$N_k = k, k_{i+1} - k_i < 0, \quad (4)$$

where $1 \leq i \leq C - 1$ and k is the number of times when the slope of the last two points is negative. The N (calculated by (3) and (4)) reflects the local “roughness” of cell boundaries. We set N as a characteristic parameter of RBC morphology.

2.5.2. Sparse Autoencoder. It has been reported that the autoencoder can add the features of active learning to the original features [43], which considerably enhance the accuracy and yield better results than the traditional classification algorithm. The autoencoder is essentially a simple data compression process, in which the encoding and decoding method is applied to compress and decompress data. In the coding stage, high-dimensional data are mapped to low-dimensional data to reduce the data size. Conversely, the decoding stage involves the reproduction of data. The sparse autoencoder (SAE), which additionally includes some sparsity constraints on the traditional autoencoder, can suppress most of the output of hidden layer neurons to achieve a sparse effect [44]. The sparsity constraint is added to make SAE better in feature representation and data reconstruction. In each layer of SSAE, the activation value h is the output of the training sample x without any label after encoding. Parameters x and h satisfy the requirement as follows [45]:

$$h = f_\theta(x) = S_f(Wx + b), \quad (5)$$

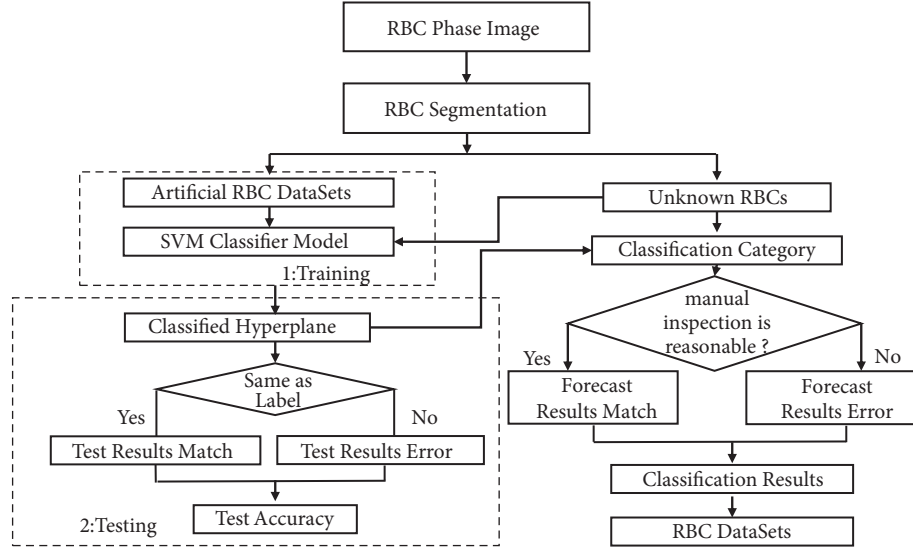


FIGURE 3: Flowchart of RBC dataset preparation based on SVM.

where S_f is the nonlinear activation function, such as the sigmoid function, W represents the weight, and b is the neuron bias. $\theta = \{W, b\}$ is the parameter set. Next, h is inversely transformed into the reconstructed representation r in the decoding process. h and r meet the requirement as follows [45]:

$$r = f_{\theta'}(h) = S_f(W'h + b'), \quad (6)$$

where $h \in ([0, 1]^d)$, $\theta' = \{W', b'\}$, W' , and W^T satisfy the relation $W' = W^T$, and W^T is the weight network between the hidden layer and the output layer, which is another characteristic parameter of RBC morphology. We constantly modify θ and θ' to minimize the average reconstruction error L by the back-propagation algorithm [26], which is calculated as follows [45]:

$$L = \|x - r\|^2. \quad (7)$$

2.6. Classifier Selection. Because the autoencoder itself is only a feature extractor and has no classification function, it is necessary to include a classifier after feature extraction to achieve classification function. In [37], the authors compared three shallow classifiers (nearest neighbor algorithm, K-nearest neighbor (KNN); back-propagation (BP) neural network; and Softmax classifier) and found that the accuracy and training time of the Softmax classifier were superior. The Softmax classifier is the expansion of the logistic regression model in multiclassification problem. It satisfies the formula as follows [46]:

$$h_{\theta}[x(i)] = \begin{bmatrix} P(y(i) = 1|x(i); \theta) \\ P(y(i) = 2|x(i); \theta) \\ \dots \\ P(y(i) = n|x(i); \theta) \end{bmatrix} = \frac{1}{\sum_{j=1}^n e^{\theta_j^T x(i)}} \begin{bmatrix} e^{\theta_1^T x(i)} \\ e^{\theta_2^T x(i)} \\ \dots \\ e^{\theta_n^T x(i)} \end{bmatrix}, \quad (8)$$

where the probability of class n being taken is as follows:

$$P_n = \frac{e^{\theta_n^T x(i)}}{\sum_{j=1}^n e^{\theta_j^T x(i)}}, \quad (9)$$

where n is the number of categories, the input value $x(i)$ is a vector, and $\theta_n^T x(i)$ represents the score value of the model in the n^{th} category of $x(i)$. The function of e is to change the score of $(-\infty, +\infty)$ to $(0, +\infty)$, which will not affect the relative size relationship. In this way, equation (9) enables a group of scores to be transformed into a group of probabilities, and the total probability is 1.

2.7. Performance Metrics. From the evaluation of the RBC classification algorithm, we annotated the true values with one-to-one circles of different colors (red, green, and blue), which represent the results of microscopic observation and RBC classification by individual experts. For quantitative evaluation of the effect of our morphological classification of RBCs, we adopted the following evaluation scheme, as shown in Figure 4:

- (1) If the observation result of experts is consistent with the algorithm prediction result, it can be considered as a correct prediction result (EE, SS, and DD), where the first E in EE is the real value and the second E is the predicted value of our algorithm. Similarly, we can obtain SS and DD.
- (2) If the observation result of experts is inconsistent with the algorithm prediction result, it can be considered as a wrong prediction result (SE, DE, ES, DS, ED, and SD), where E represents the echinocyte, S represents the spherocyte, and D represents the discocyte. The upper left corner of Figure 4 shows the possible predictive results of the three shapes of RBCs, where green, red, and blue circles represent the discocyte, echinocyte, and spherocyte detected manually, respectively. In addition, green, red, and

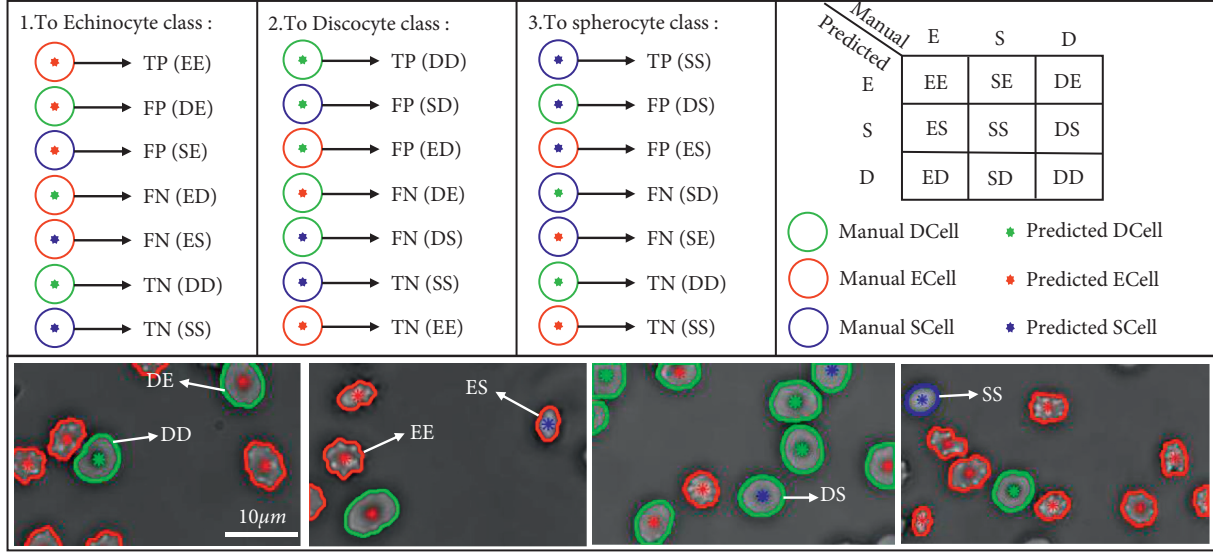


FIGURE 4: The confusion matrix shown on the top right for one-to-one matching evaluation is used to evaluate the accuracy of RBC classification detection. The figure in the upper left corner shows examples of DD, DE DS, ED, EE, ES, SD, SE, and SS. For point correspondence, we do not use specificity or true negative (TN) rate because most image pixels are TN.

blue dots are the predicted cell categories for the RBCs. The confusion matrix [47] in the upper right corner of Figure 4, also known as error matrix, a common method to evaluate the performance of classifiers, depicts the relationship between the real attributes of the sample and the prediction results. Examples of the RBC classification results obtained in this study are shown in Figure 4, which highlights the cases of misclassification.

To quantitatively analyze the quality of the DNN, we applied accuracy and F1 measure to evaluate the classification results, as shown in the model evaluation box in Figure 3. Recall is a statistical measurement to quantify the ability of an algorithm to classify objects automatically. Different categories of recall are expressed as $Rec(E) = EE/(EE + ES + ED)$, $Rec(S) = SS/(SE + SS + SD)$, and $Rec(D) = DD/(DE + DS + DD)$, respectively. Different categories of precision are $Pre(E) = EE/(EE + SE + DE)$, $Pre(S) = SS/(SE + SS + SD)$, and $Pre(D) = DD/(DE + DS + DD)$, respectively, which are used to evaluate the robustness of the algorithm in avoiding misclassification. The F1 measure is the harmonic average value of precision and recall, which satisfies the requirement $F1 = 2 \times (Rec \times Pre)/(Rec + Pre)$. In addition, we used the index of accuracy to evaluate this RBC classification model, which is estimated as follows:

$$Accuracy = \frac{EE + SS + DD}{Num}, \quad (10)$$

where Num is the total number of classified RBCs. The index of misclassification rate (MR) [19] is then calculated as follows:

$$MR = 1 - accuracy. \quad (11)$$

3. Experimental Results

3.1. Morphological Differentiation of RBCs by Bright Field Imaging and QPI. It is difficult to observe the details of unstained RBCs by traditional bright field (BF) imaging technology because of the poor contrast of transparent and translucent samples. To improve the image contrast of RBC samples, we used QPI technology for microscopic imaging of unstained RBCs. First, according to the illumination angles of the left and right half of LED arrays, two oblique illumination images were captured by CCD, as shown in Figures 5(a1) and 5(a2). Second, the left and right complementary oblique illumination images were then transformed into the left-right DPC image (Figure 5(b1)) by equation (1). The top and bottom oblique illumination images are shown in Figures 5(a3) and 5(a4), and the top-bottom DPC image is shown in Figure 5(b2) in the same way. Finally, QPI image (Figure 5(d)) was restored by DPC images using phase transfer function (equation (2)). To further visualize the three-dimensional structure of QPI, mesh of RBC was calculated by the mesh function and view function [48]. To better observe the two-dimensional structure of the mesh image, we set the azimuth and elevation to 0 and -88, respectively. Figure 5(c) shows the RBCs in BF. Echinocytes with rough edges can be clearly observed, but the morphological characteristics of discocytes and spherocytes are not apparent. Compared to the BF images, the different shapes of RBCs was distinguished according to different phase information [15] in QPI images.

3.2. Segmentation and Recognition of RBC Using QPI. To achieve RBC classification, the RBCs were segmented, and each RBC was then extracted from the segmented RBC phase

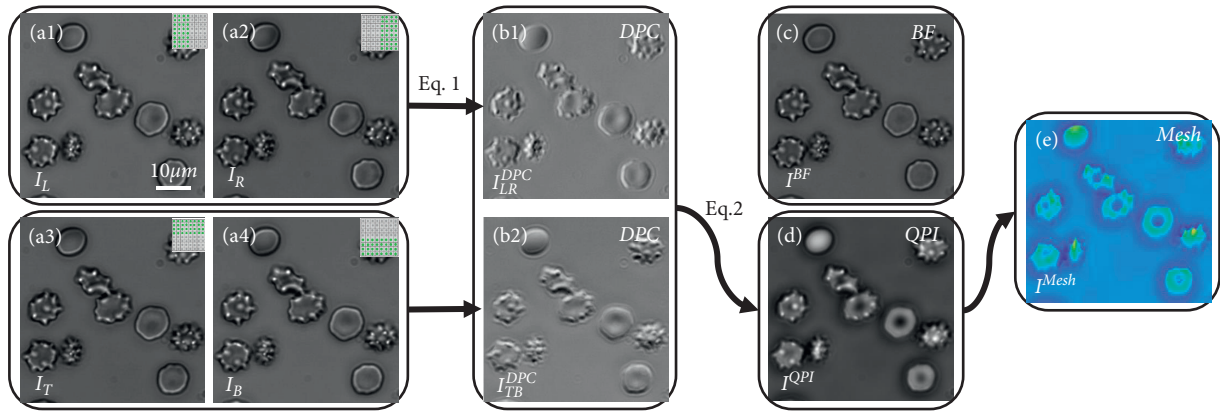


FIGURE 5: QPI visualization and BF images of RBCs (a1)–(a4) are the oblique illumination images of the LED array in the left, right, top, and bottom illuminations, respectively; (b1)–(b2) are the left-right and top-bottom DPC images, respectively; (c) RBC bright field image; (d) reconstructed QPI; (e) mesh of QPI. The upper right corner of the picture shows the lighting mode of the LED array.

image. The segmentation and extraction results are shown in Figure 6, displaying preprocessing results, RBC segmentation analyzed by the relatively simple Otsu method [35], and RBC extraction in different imaging modes. Images in the first line of Figure 6 are the preprocessed microscopic images of RBCs in the same field of view, including BF, OI, DPC, QPI, and mesh of QPI. Images in the second line of Figure 6 are the binary images of RBCs in five imaging modes. The comparison revealed that QPI highlighted by mesh show better morphological characteristics and clearer cell contour of RBCs than BF, OI, and DPC. Here, mesh displays the pseudocolor and pseudostereo effect of QPI. Images in the last line of Figure 6 show the results of cell edge extraction under five imaging modes, where the RBC edge extraction effects of QPI and mesh are better in RBC phase images with several slightly adherent RBCs [49, 50] than BF, OI, and DPC. These results show that the images of QPI have better segmentation performance than those of DPC via the same segment algorithm. This is convenient for subsequent single RBC extraction.

3.3. Dataset Based on SVM. The three shapes of RBC samples were selected by experienced biologist experts: discocytes (105 samples) with relatively circular depression area, echinocytes (102 samples) with locally uneven and irregular boundary, and spherocytes (100 samples) without relatively circular depression area. The images of these samples were input into SVM being trained to form the classification hyperplane, and then, a large number of segmented single RBCs were tested by the hyperplane for the preparation of RBC datasets. To further determine the quality of the datasets, RBC datasets prepared by SVM needed the manual review by two professionals. Figure 7 shows some examples of the datasets of the three shapes of RBCs predicted by SVM. The process of predicting and reviewing 100 cells through our method took 30 seconds. As a comparison, it took approximately 167 seconds to prepare a dataset of 100 cells by the manual preparation method.

3.4. Boundary Curvature Improving the Accuracy of RBC Classification. The measurement based on the morphological analysis of RBCs may provide a possible alternative analysis method [1, 14] to replace the measurement of hemoglobin concentration on determining blood quality [51]. Morphological analysis of the different shapes of RBCs in BF and QPI is shown in Figure 8. Figures 8(a) and 8(b) show the BF and QPI images of RBCs, respectively. Figures 8(c) and 8(d) are the local images of Figures 8(a) and 8(b), respectively, where cells A, B, and C represent the spherocyte, echinocyte, and discocyte, respectively. Figure 8(e) shows BCs of the three shapes of RBCs in BF and QPI and the corresponding mesh; the figure shows that BC can separate cell B from RBCs with smooth boundary (cells A and C) because N mentioned in (4) of cell B is larger than that of cells A and C whether in BF or QPI. Contrary to the regular morphological characteristics of discocytes and spherocyte, the boundaries of echinocytes are irregular with variations, which may lead to incomplete morphological feature learning and even affect the final classification results. Thus, to reduce the misclassification rate of RBCs, we set the number of negative values, N , of BC as the threshold for the preliminary classification of echinocyte-shaped RBCs from RBCs with smooth boundaries (discocyte and spherocyte) before training and learning. The influence of BC on the results of RBC classification in BF and QPI is shown in Figure 9. Figures 9(a) and 9(b) show the RBC classification without BC and with BC in BF, respectively. Figures 9(c) and 9(d) show the RBC classification without BC and with BC in QPI, respectively. These figures show that BC can avoid situations where echinocyte-shaped RBCs are misclassified as discocytes or spherocytes in BF and QPI, as shown in yellow and green boxes of Figure 9. The average MR calculated by (11) is 7.1% without BC, and the average MR is 5% with BC (the average MR has been reduced by 2.1%). In addition, compared to BF, QPI can reduce the probability that spherocytes are misclassified as discocytes, as shown in white boxes of Figure 9. The basic RBC classification relies on SSAE and Softmax classifiers, and QPI and BC jointly improve the accuracy of RBC classification.

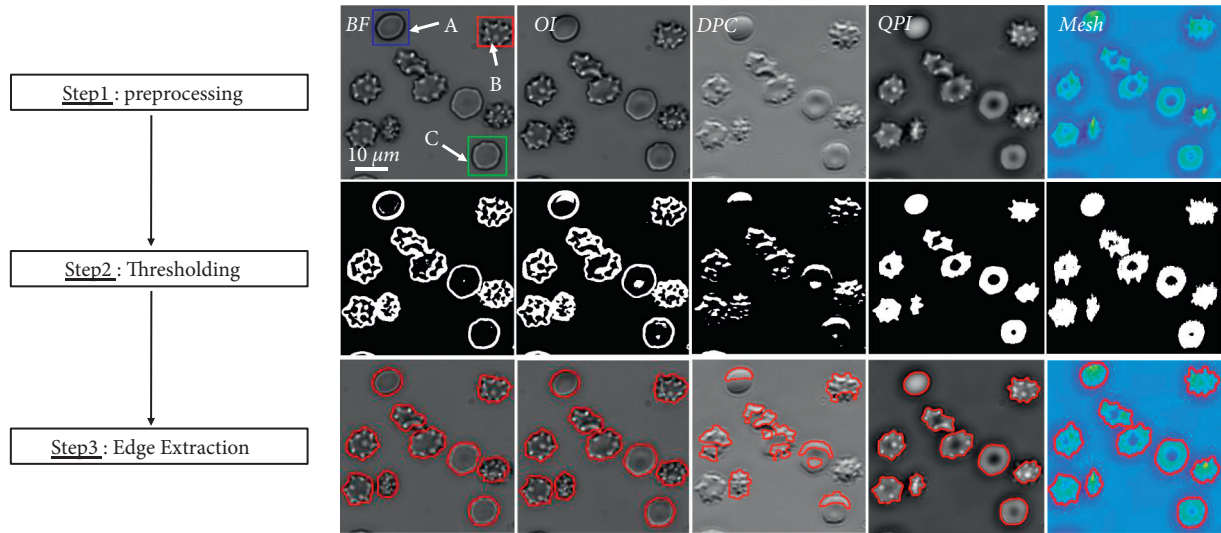


FIGURE 6: Segmentation and extraction effect of RBCs in different imaging modes. The images in the first line are preprocessing results of BF, OL, DPC, QPI, and mesh, where A, B, and C are the spherocyte, echinocyte, and discocyte, respectively. The images in the second line are thresholding results processed by the Otsu method. The images in the third line are edge extraction results processed by thresholding results, where the extracted cell edges are marked with red points.

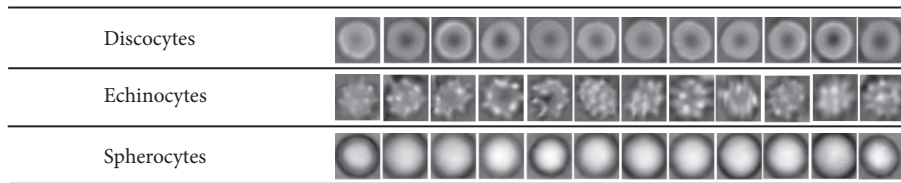


FIGURE 7: Examples of the three shapes of RBCs.

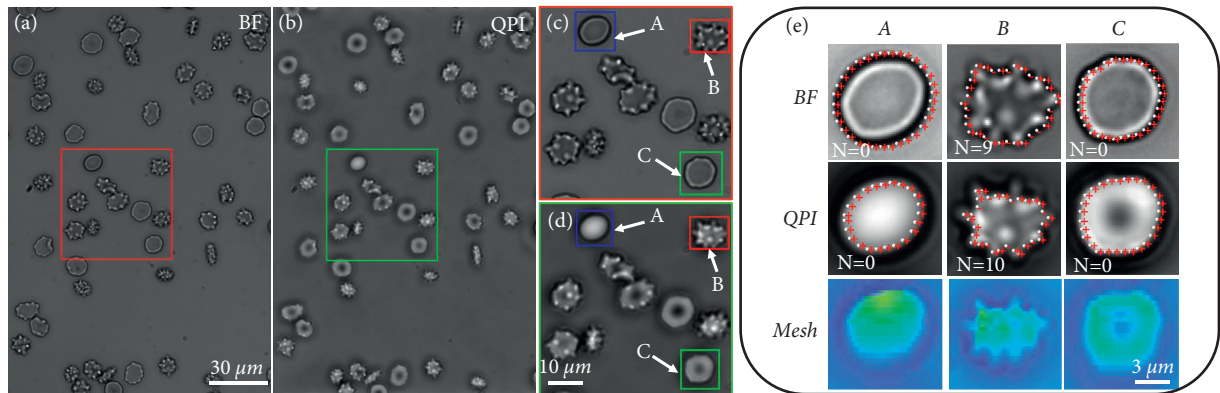


FIGURE 8: Morphological analysis of the different shapes of RBCs in BF and QPI. (a) RBC BF image. (b) RBC QPI image. (c) Local image as shown in the red box of (a). (d) Local image as shown in the green box of (b). (e) BCs of the three shapes of RBCs in BF and QPI and their mesh form, where the white dots of A, B, and C are the equally spaced sampling points of cell boundary, red marks “+” represents positive value of BC, red marks “-” represents the negative value of BC, and N is the number of negative values of BC mentioned in equation (4).

3.5. SSAE. Datasets of the different shapes of RBCs were input into the DNN for training and testing. The quality of the model largely affects the final result, and the accuracy is used to evaluate the quality of the model (10) [47]. The sparsity proportion, sparsity regularization, L2 weight regularization, and iterations in the SAE affect the accuracy of the DNN [52]. To verify the influence of these four parameters on the accuracy of the DNN, we adjusted one of the

parameters to optimize the accuracy. Figure 10 shows the relationship between different parameters and accuracy. Initially, we changed the parameter sparsity proportion, while leaving the other three parameters unchanged. We set iterations of the single-layer SAE and Softmax layer as 10, the number of hidden neurons of the SAE as 100, and the two parameters of sparse regularization and L2 weight regularization as 4 and 0.004, respectively. The results

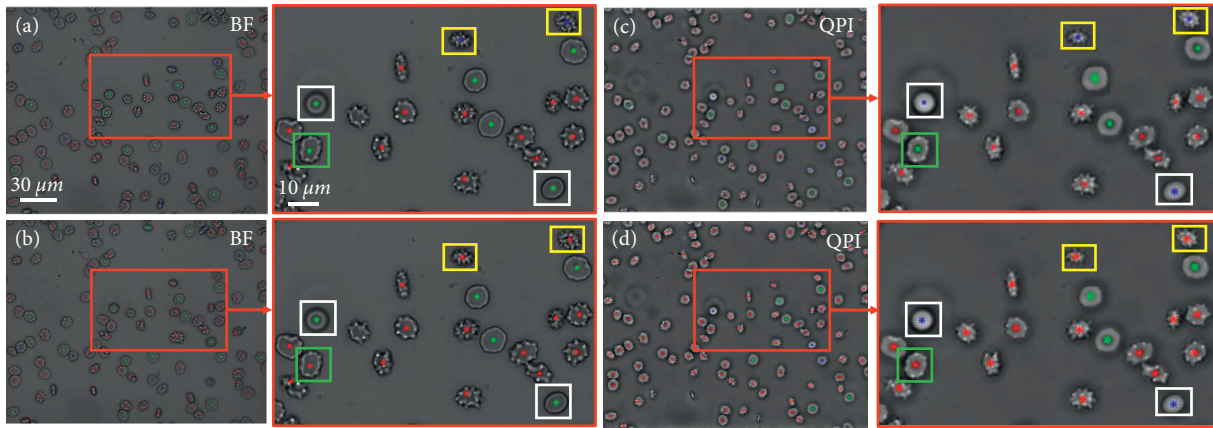


FIGURE 9: The influence of BC on the results of RBC classification in BF and QPI. (a) RBC classification without BC in BF. (b) RBC classification without BC in QPI. (c) RBC classification with BC in BF. (d) RBC classification with BC in QPI. Red, green, and blue dots indicate that the predicted results are echinocyte-shaped RBCs, discocyte-shaped RBCs, and spherocyte-shaped RBCs, respectively.

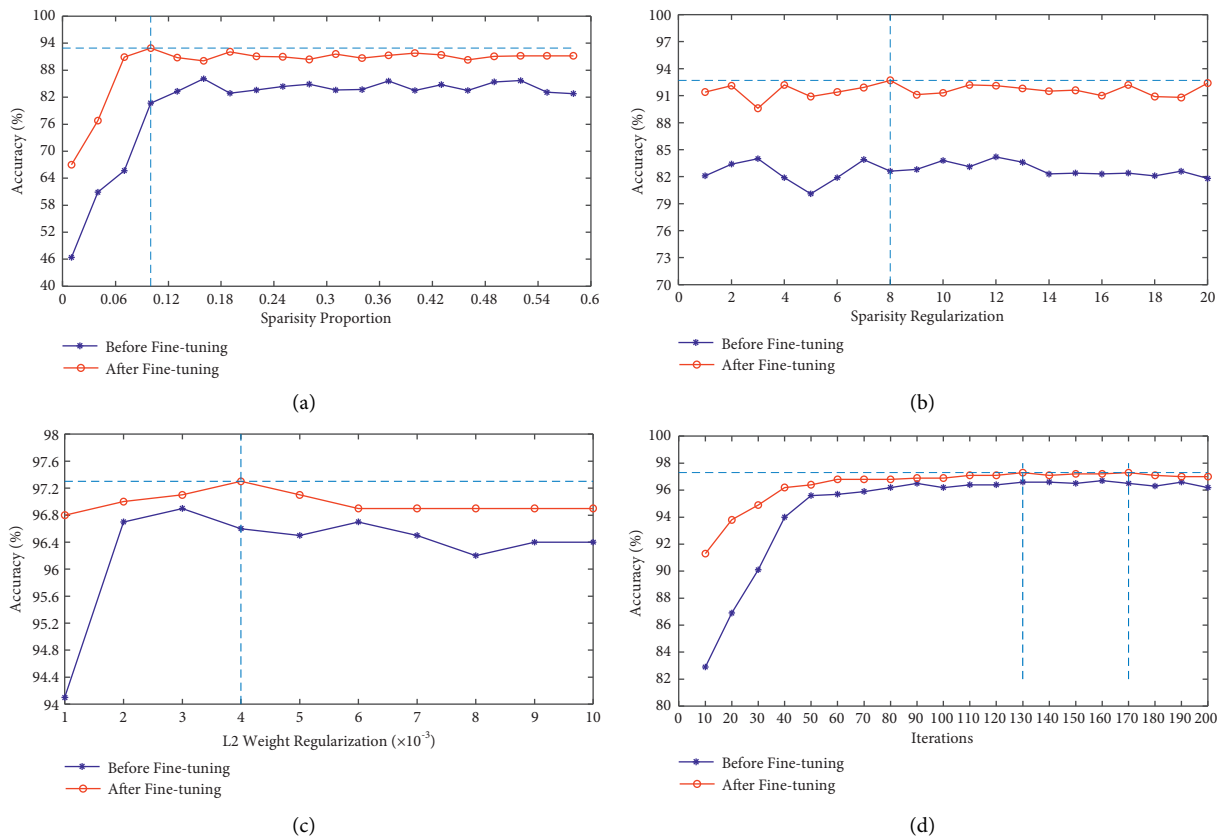


FIGURE 10: The relationship between different parameters and the accuracy of SSAE. (a) The influence of sparsity proportion on model accuracy. (b) The influence of sparse regularization on model accuracy. (c) The influence of L2 weight regularization on model accuracy. (d) The influence of iterations on model accuracy. The blue and red curves are the curves before and after fine tuning, respectively.

revealed that the accuracy was the highest when the sparsity proportion was 0.10, as shown in Figure 10(a). Next, according to the above best parameters, we changed the parameter sparsity regularization while leaving the other three parameters unchanged. We set the number of iterations of the single-layer SAE and Softmax layer as 10, the number of hidden neurons in SAE as 100, and the sparsity

proportion and L2 weight regularization to 0.10 and 0.004, respectively. The results revealed that the accuracy was the highest when sparsity regularization was 8, as shown in Figure 10(b). Then, according to the above best parameters, we changed the parameter L2 weight regularization while leaving the other three parameters unchanged. We set iterations of the single-layer SAE and Softmax layers as 10, the

TABLE 1: Parameter values of the algorithm in this article.

	Number of hidden neurons	Maximum times of iterations	Value of L2 regularization	Value of sparse regularization	Proportion of sparsity
SAE1	100	130	0.004	8	0.10
SAE2	50	70	0.004	8	0.10
Softmax layer	—	130	—	—	—

TABLE 2: RBC classification based on our method.

RBC phase image	Number of cells observed	Predicted group			Actual group			MR (%)	Time (s)
		E	S	D	E	S	D		
1.jpg	114	98	5	11	99	2	13	7.9	4
2.jpg	153	143	2	0	148	2	3	4.6	5
3.jpg	148	80	5	63	88	0	60	8.8	5
4.jpg	127	80	5	42	80	0	47	9.4	5
5.jpg	49	0	49	0	0	49	0	0	4
6.jpg	46	0	46	0	0	46	0	0	3

number of hidden neurons of the SAE as 100, and sparsity proportion and sparsity regularization as 0.10 and 8, respectively. The accuracy was found to be the highest when L2 weight regularization was 0.004, as shown in Figure 10(c). Finally, according to the above best parameters, we changed the parameter iterations while leaving the other three parameters unchanged. We set the number of hidden neurons of SAE as 100 and the three parameters of sparsity proportion, sparsity regularization, and L2 weight regularization as 0.10, 8, and 0.004, respectively. The DNN with 130 and 170 iterations exhibited the highest accuracy, as shown in Figure 10(d). The red and blue curves in Figure 10 show that the accuracy can be further increased by fine tuning, namely, by initializing the network weight according to the original model parameters, optimizing the network parameters using the back-propagation algorithm [26], and minimizing L of equation (7). In [53], the authors reported that SSAE could further learn the features of the dataset and reduce feature dimension. Therefore, we selected SSAE formed by stacking the traditional two-layer SAEs plus Softmax classifier and further fine-tuned to form the DNN. Since the greater the number of iterations, the longer the training time. After several experiments, we chose the parameters with best performance in all experiments, and the values of each parameter are given in Table 1.

4. Discussion

Based on the above parameter settings, the datasets of the three shapes of RBC were input into SSAE composed of a two-layer SAEs plus Softmax classifier for training by fine tuning to form the DNN. If p (equation (9)) was greater than 0.5, the prediction matching of the category result was successful. In contrast, the predictions did not match if the mapping probability was less than 0.5. Repeat the prediction three times for any RBC phase images according to the RBC classification process shown in Figure 1. Table 2 provides the final average classification results of six RBC phase images, where E, S, and D are the echinocyte, spherocyte, and discocyte, respectively.

Table 2 provides that our RBC classification scheme that relies only on the phase information on RBC itself is a good RBC classification method, where MR calculated by (11) is less than 10%, and the cell detection time is approximately 20 cells per second. Similarly, we input the same RBC phase images into the convolutional neural network (CNN) [17] that was trained by the same RBC datasets. The classification results, MR, and cell detection time of the three shapes of RBCs are given in Table 3. Compared to the classification results outcome by our developed model, the MR and the average time of cell detection of the CNN were relatively higher (5% and >3.2 s, respectively), especially for samples with more discocytes. We compared the classification of discocytes (D), and our method had significantly improved the classification accuracy for large numbers of cells, which corresponded the case of various clinical assays.

We also used model accuracy [47] to compare our proposed method with the CNN. For the RBC classification algorithm, our model accuracy was 0.973, which was higher than that of the CNN (0.940). In addition, the F1 measure of our RBC classification method was 3.3% higher than the CNN. CNN-based feature representation involves convolution and subsampling operations to learn a set of locally connected neurons through the local receptive fields for feature extraction [18], while SSAE is a full connection model that learns a single global weight matrix for feature representation [30]. SSAE is trained in a bottom-up unsupervised manner to extract hidden features. Compared to the CNN, SSAE achieves higher accuracy with less processing time for training using the same dataset, as shown in the model accuracy (equation (10)) and the results given in Tables 2 and 3.

Although the data augmentation of RBC phase images was used, it was still difficult to increase the performance of our proposed model as not all echinocytes could be trained and learned due to the diversity and irregularity of echinocyte morphology. Moreover, only discocytes, echinocytes, and spherocytes were considered in this work. In the future, our study will involve more shapes of training samples and explore the RBCs classification methods of other suitable

TABLE 3: Classification of RBCs based on the CNN [17].

RBC phase image	Number of cells observed	Predicted group			Actual group			MR (%)	Time (s)
		E	S	D	E	S	D		
1.jpg	114	83	2	28	99	2	13	7.0	8
2.jpg	153	146	3	4	148	2	3	5.2	11
3.jpg	148	67	0	82	88	0	60	9.4	11
4.jpg	127	37	0	90	80	0	47	15.0	9
5.jpg	49	0	49	0	0	49	0	0	3
6.jpg	46	0	46	0	0	46	0	0	3

feature values, such as texture inhomogeneity and border roughness [12], to further increase the performance. Since QPI technology provides the phase information that can reveal microstructures compared with intensity imaging for unstained cells, our classification method could be applied to various unstained tissue slices of specific recognition. Thus, our proposed method could be potentially used for other real-time applications.

5. Conclusions

In this study, we proposed a method for automatic classification of RBC morphology based on QPI. First, compared with the traditional bright field image, QPI delivers better image for analysis of unstained RBCs. Second, the watershed algorithm based on the connected domain analysis is used to show that QPI is more conducive to the segmentation and recognition of RBCs. Third, compared with the manual dataset, the dataset preparation method based on SVM can avoid the manual subjective error and thus increase the efficiency. Last, the morphological features extracted by BC and SSAE can be classified by the Softmax classifier, and the misclassification rate of RBCs can be reduced by BC. The experimental results show that our classification method can achieve automatic classification of RBC morphology based on QPI, with high accuracy, minimal calculation, fast recognition speed, and no requirement to set the feature selection parameters artificially. In addition, our classification method has the potential to be applied to analysis of RBC-related diseases and evaluation of the quality of long-term stored RBCs.

Abbreviations

RBCs:	Red blood cells
QPI:	Quantitative phase imaging
DHM:	Digital holography microscopy
DPC:	Differential phase contrast
TIE:	Transport of intensity equation
OI:	Oblique illumination
SSA:	Stacked sparse autoencoder
SAE:	Sparse autoencoder
BC:	Boundary curvature
CCD:	Charge-coupled device
WOTF:	Weak object transfer function
PBS:	Phosphate buffer saline
SVM:	Support vector machine
KNN:	K-nearest neighbor

BP:	Back-propagation
DNN:	Deep neural network
MR:	Misclassification rate
BF:	Bright field
CNN:	Convolutional neural network
TN:	True negative.

Data Availability

The data used to support the findings of this study are included within the supplementary material.

Conflicts of Interest

The authors declare no that they have no conflicts of interest.

Authors' Contributions

Mengduo Jiang and Meng Shao contributed equally to this work.

Acknowledgments

This research was supported by the Natural Science Foundation of Anhui Province in China (1908085MA14) and the Project of Research Fund of Anhui Institute of Translational Medicine (2021zhyx-B16).

Supplementary Materials

The supplementary material includes training data and testing data. The training data are 10800 (3600 for each shape RBCs) single 50×50 RBC phase images used for training, and the testing data include 3600 (1200 for each shape RBCs) single 50×50 RBC phase images. Six 1920×1080 RBC phase images were used for RBC morphology classification. All phase images are in .jpg format. (*Supplementary Materials*)

References

- [1] D. A. Sierra Fajardo, "Flow Cytomorphometry for Assessment of Red Blood Cell Storage Lesion," vol. 11, Mannheim University, Mannheim, Germany, 2017.
- [2] J. F. Flatt, W. M. Bawazir, and L. J. Bruce, "The involvement of cation leaks in the storage lesion of red blood cells," *Frontiers in physiology*, vol. 5, p. 214, 2014.
- [3] T. Kirkwood, "Cellular aging and cell death," *British Journal of Cancer*, vol. 76, no. 1, p. 138, 1997.
- [4] I. Moon, F. Yi, Y. H. Lee, B. Javidi, D. Boss, and P. Marquet, "Automated quantitative analysis of 3D morphology and

- mean corpuscular hemoglobin in human red blood cells stored in different periods,” *Optics Express*, vol. 21, no. 25, pp. 30947–30957, 2013.
- [5] J. Yong, R. Ping, B. Feng, D. Endocrinology, and G. University, “The changes and clinical significance in morphological structure and membrane elasticity of red blood cells in T2DM patients,” *Chinese Journal of Diabetes*, vol. 21, pp. 998–1001, 2013.
 - [6] Z. Xu, Y. Zheng, X. Wang, N. Shehata, C. Wang, and Y. Sun, “Stiffness increase of red blood cells during storage,” *Microsystems & Nanoengineering*, vol. 4, no. 1, Article ID 17103, 2018.
 - [7] D. J. Triulzi and M. H. Yazer, “Clinical studies of the effect of blood storage on patient outcomes,” *Transfusion and Apheresis Science*, vol. 43, no. 1, pp. 95–106, 2010.
 - [8] C. C. Hortinela, J. R. Balbin, J. C. Fausto, P. D. C. Divina, and J. P. T. Felices, “Identification of abnormal red blood cells and diagnosing specific types of anemia using image processing and support vector machine,” in *Proceedings of the IEEE 11th International Conference on Humanoid, Nanotechnology, Information Technology, Communication and Control, Environment, and Management (HNICEM)*, pp. 1–6, Laoag, Philippines, Nov.-Dec. 2019.
 - [9] L. Alzubaidi, O. Al-Shamma, M. A. Fadhel, L. Farhan, and J. Zhang, “Classification of red blood cells in sickle cell anemia using deep convolutional neural network,” in *Proceedings of the International Conference on Intelligent Systems Design and Applications*, Springer, Tokyo, Japan, April 2019.
 - [10] H. A. Abdulkarim, M. A. Abdul Razak, R. Sudirman, and N. Ramli, “A deep learning AlexNet model for classification of red blood cells in sickle cell anemia,” *IAES International Journal of Artificial Intelligence*, vol. 9, no. 2, pp. 221–228, 2020.
 - [11] J. A. Akrimi, A. Suliman, L. E. George, and A. R. Ahmad, “Classification red blood cells using support vector machine,” in *Proceedings of the 6th International Conference on Information Technology and Multimedia*, pp. 265–269, Putrajaya, Malaysia, November 2014.
 - [12] H. A. Elsalamony, “Healthy and unhealthy red blood cell detection in human blood smears using neural networks,” *Micron*, vol. 83, pp. 32–41, 2016.
 - [13] S. H. Shirazi, A. I. Umar, N. Haq, S. Naz, M. I. Razzak, and A. Zaib, “Extreme learning machine based microscopic red blood cells classification,” *Cluster Computing*, vol. 21, no. 1, pp. 691–701, 2017.
 - [14] D. A. F. Sierra, K. A. Melzak, K. Janetzko et al., “Flow morphometry to assess the red blood cell storage lesion,” *Cytometry, Part A*, vol. 91, no. 9, pp. 874–882, 2017.
 - [15] H. Lee and Y.-P. P. Chen, “Cell morphology based classification for red cells in blood smear images,” *Pattern Recognition Letters*, vol. 49, pp. 155–161, 2014.
 - [16] F. Yi, I. Moon, and B. Javidi, “Automated red blood cells extraction from holographic images using fully convolutional neural networks,” *Biomedical Optics Express*, vol. 8, no. 10, pp. 4466–4479, 2017.
 - [17] J. L. Wang, A. Y. Li, A. K. Ibrahim, H. Zhuang, and A. Mu Ha Med, “Classification of white blood cells with pattern net-fused ensemble of convolutional neural networks (PECNN),” in *Proceedings of the IEEE International Symposium on Signal Processing and Information Technology 2018*, pp. 325–330, Louisville, KY, USA, Dec. 2018.
 - [18] I. Moon and K. Jaferzadeh, “Holographic red blood cell image analysis,” in *Proceedings of the 17th Workshop on Information Optics (WIO)*, pp. 1–2, Quebec, QC, Canada, July 2018.
 - [19] F. Yi, I. Moon, and B. Javidi, “Cell morphology-based classification of red blood cells using holographic imaging informatics,” *Biomedical Optics Express*, vol. 7, no. 6, pp. 2385–2399, 2016.
 - [20] Y. Xu, Y. Wang, W. Jin, C. Lv, and H. Wu, “A new method of phase derivative extracting for off-axis quantitative phase imaging,” *Optics Communications*, vol. 305, pp. 13–16, 2013.
 - [21] E. Ahmadzadeh, K. Jaferzadeh, J. Lee, and I. Moon, “Automated three-dimensional morphology-based clustering of human erythrocytes with regular shapes: stomatocytes, discocytes, and echinocytes,” *Journal of Biomedical Optics*, vol. 22, Article ID 76015, 2017.
 - [22] X. He, “Research On Multi-mode Microscopic Imaging Technology Of Brightfield, Darkfield, Phase Contrast,” vol. 6, University of Electronic Science and Technology of China, Sichuan, China, 2017.
 - [23] C. Zuo, Q. Chen, S. Sun Jiasong, and A. Asundi, “Non-interferometric phase retrieval and quantitative phase microscopy based on transport of intensity equation: a review,” *Chinese Journal of Lasers*, vol. 43, no. 6, Article ID 0609002, 2016.
 - [24] K. Jaferzadeh and I. Moon, “Human red blood cell recognition enhancement with three-dimensional morphological features obtained by digital holographic imaging,” *Journal of Biomedical Optics*, vol. 21, no. 12, Article ID 126015, 2016.
 - [25] R. Sugimoto, R. Maruyama, Y. Tamada, H. Arimoto, and W. Watanabe, “Contrast enhancement by oblique illumination microscopy with an LED array,” *Optik*, vol. 183, pp. 92–98, 2019.
 - [26] J. Chen, Y. Rong, Q. Zhu, B. Chandra, and H. Zhong, “A generalized minimal residual based iterative back propagation algorithm for polynomial nonlinear models,” *Systems & Control Letters*, vol. 153, Article ID 104966, 2021.
 - [27] L. Tian and L. Waller, *Quantitative Phase Imaging*, SPIE, San Francisco, California, USA, 2015.
 - [28] W. H. Reinhart and S. Chien, “Echinocyte-stomatocyte transformation and shape control of human red blood cells: morphological aspects,” *American Journal of Hematology*, vol. 24, no. 1, pp. 1–14, 1987.
 - [29] N. Safca, P. Dan, L. Ichim, H. Elkhatib, and O. Chenaru in *Proceedings of the 22nd International Conference on System Theory, Control and Computing (ICSTCC)*, pp. 93–98, Sinaia, Romania, October 2018.
 - [30] A. Kumar, B. R. Schmidt, Z. A. C. Sanchez et al., “Automated motion tracking and data extraction for red blood cell biomechanics,” *Current Protocols in Cytometry*, vol. 93, p. e75, 2020.
 - [31] G. Liu, “Based on the horizontal noise elimination of medical adhesion image edge segmentation algorithm,” *Bulletin of Science and Technology*, vol. 29, pp. 91–93, 2013.
 - [32] J. Huang, “An improved algorithm of overlapping cell division,” in *Proceedings of the International Conference on Intelligent Computing and Integrated Systems*, pp. 687–691, Guilin, China, October 2010.
 - [33] J. J. Zhao, H. Yu, X. G. Gu, and S. Wang, “The edge detection of river model based on self-adaptive Canny Algorithm and connected domain segmentation,” in *Proceedings of the 8th World Congress on Intelligent Control and Automation*, pp. 1333–1336, A separating algorithm for overlapping red blood cell images, Jinan, China, July 2010.
 - [34] C. Tornasi and R. Manduchi, “Bilateral filtering for gray and color images,” in *Proceedings of the IEEE International Conference on Computer Vision*, pp. 839–846, Bombay, India, January 1998.

- [35] Y. You and H. Yu, *Journal of Image Graphics*, vol. 10, pp. 736–740, 2005.
- [36] B. Atal and M. Schroeder, “Predictive coding of speech signals and subjective error criteria,” *IEEE Transactions on Acoustics, Speech, & Signal Processing*, vol. 27, no. 3, pp. 247–254, 1979.
- [37] H. E. Li, K. Han, and Y. Liu, “Self-adaptive SVM incremental learning algorithm,” *Journal of Frontiers of Computer Science and Technology*, vol. 127, pp. 111–120, 2019.
- [38] L. Alzubaidi, M. A. Fadhel, O. Al-Shamma, J. Zhang, and Y. Duan, “Deep learning models for classification of red blood cells in microscopy images to aid in sickle cell anemia diagnosis,” *Electronics*, vol. 9, no. 3, p. 427, 2020.
- [39] S. Chandrasiri and P. Samarasinghe, “Morphology based automatic disease analysis through evaluation of red blood cells,” in *Proceedings of the 2014 5th International Conference on Intelligent Systems, Modelling and Simulation*, pp. 318–323, Langkawi, Malaysia, January 2014.
- [40] S. Pettitt, “Passion on the surface but missing a heartbeat,” *Proceedings of SPIE - The International Society for Optical Engineering*, vol. 5421, pp. 172–182, 2004.
- [41] R. Grebe and H. Schmid-Schönbein, “Tangent counting for objective assessment of erythrocyte shape changes,” *Biorheology*, vol. 22, no. 6, pp. 455–469, 1985.
- [42] R. C. Gonzale and R. E. Woods, *Digital Image Processing*, p. 527, Third edition, Publishing House of Electronics Industry, Beijing, China, 2009.
- [43] W. J. Jia and Y. D. Zhang, “Survey on theories and methods of autoencoder,” *Computer Systems Applications*, vol. 27, pp. 1–9, 2018.
- [44] F. Yuan, L. Zhang, J. Shi, X. Xia, and G. Li, “Theories and application of Auto-Encoder neural network: a literature survey,” *Chinese Journal of Computers*, vol. 42, pp. 203–230, 2019.
- [45] S. Lin, H. Sheng, and Q. Li, “Handwritten digital classification based on the stacked sparse autoencoders,” *Microprocessors*, vol. 36, pp. 47–51, 2015.
- [46] J. Wang, Y. Jia, and X. Zhao, *Tobacco Science Technology*, pp. 18–22, 2014.
- [47] J. T. Feng, “The Research on Human Activity Recognition Based on Ensemble Model,” Zhejiang University, Hangzhou, China, 2017.
- [48] S. Bohn, M. Fetisova, M. Agsten, A. K. Marten, and D. Westermann, “A continuous DC voltage control function for meshed HVDC grids, and the impact of the underlying future AC grid due to renewable in-feed,” in *Proceedings of the 2014 International Conference on Modelling, Identification & Control*, pp. 6–11, Melbourne, VIC, Australia, December 2014.
- [49] Q. Quan, J. Wang, and L. Liu, “An effective convolutional neural network for classifying red blood cells in malaria diseases,” *Interdisciplinary Sciences: Computational Life Sciences*, vol. 12, pp. 1–9, 2020.
- [50] S. Zafari, M. Murashkina, T. Eerola, J. Sampo, H. Kälviäinen, and H. Haario, “Resolving overlapping convex objects in silhouette images by concavity analysis and Gaussian process,” *Journal of Visual Communication and Image Representation*, vol. 73, Article ID 102962, 2020.
- [51] E. Schapkaitz and S. Raburabu, “Performance evaluation of the new measurement channels on the automated Sysmex XN-9000 hematology analyzer,” *Clinical Biochemistry*, vol. 53, pp. 132–138, 2018.
- [52] W. Jia, K. Muhammad, S.-H. Wang, and Y.-D. Zhang, “Five-category classification of pathological brain images based on deep stacked sparse autoencoder,” *Multimedia Tools and Applications*, vol. 78, no. 4, pp. 4045–4064, 2019.
- [53] T.-H. Song, V. Sanchez, H. Ei Daly, and N. M. Rajpoot, “Simultaneous cell detection and classification in bone marrow histology images,” *IEEE Journal of Biomedical and Health Informatics*, vol. 23, no. 4, pp. 1469–1476, 2019.